5.24

Modelling and Simulation of the Portevin-Le Chatelier Effect

C. Brüggemann[1], T. Böhlke[2], and A. Bertram[1]

[1] Institut für Mechanik, Otto-von-Guericke-Universität Magdeburg
[2] Institut für Technische Mechanik, Universität Karlsruhe (TH)

Abstract. During deformations of an Al-Mg alloy (AA5754) dynamic strain aging occurs in a certain range of temperatures and strain-rates. A manifestation of this phenomenon, usually referred to as the Portevin-Le Chatelier (PLC) effect, consists of the occurrence of strain localisation bands accompanied by discontinuous yielding. The PLC effect is due to dynamic dislocation-solute interactions and results in negative strain-rate sensitivity of the flow stress. The PLC effect is detrimental to the surface quality of sheet metals and also affects the ductility of the material. Since the appearance of the PLC effect strongly depends on the tri-axiality of the stress state, three-dimensional finite element simulations are necessary in order to optimise metal forming operations. We present a geometrically non-linear material model which reproduces the main features of the PLC effect. The material parameters are identified by experimental data from tensile tests. Special emphasis is put on the prediction of the critical strain for the onset of the PLC effect and the statistical characteristics of the stress drop distribution.

1 Physical and Mechanical Characteristics of the PLC Effect

The material instability called PLC effect is a special type of dynamic strain aging, which is observed during deformation processes of, e.g., Al, Fe, Cu, and Ni base alloys. This effect describes the discontinuous yielding in strain localisation or shear bands (Fig. 1 left). While the deformation process initially begins in a stable manner, instantaneously shear bands appear in dependence of the deformation rate and temperature. For special alloys the critical strain for the onset of the PLC effect is minimal for special strain rates, while for smaller or greater strain rates the PLC effect occurs later in process, which is called inverse and normal behaviour, respectively (Fig. 1 right). Strain localisations produce a typical serrated material response in the stress strain curves of tensile tests. In stress driven tests steps are observed in the stress-strain curve. However, for strain rate driven tests the serrations have different statistical characteristics in dependence of the applied strain rate, and so one typically distinguishes three different types (Fig. 1 middle)

A: high strain rate - stochastic development of bands over the hole specimen
B: medium strain rate - hopping bands
C: low strain rate - the PLC-band goes continuously through the specimen

As a consequence, the material quality is reduced, which is manifested in a loss of ductility and a reduction of the surface quality of the deformed part. In Figure 1 (left)

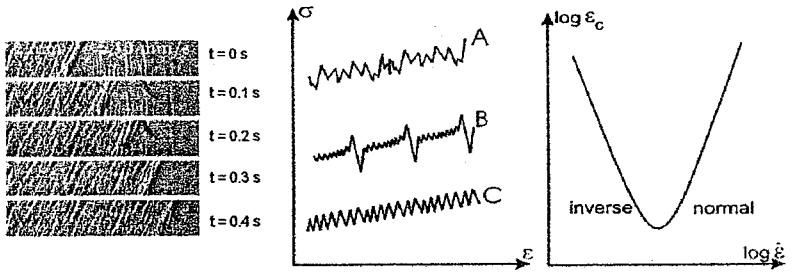

Fig. 1. Localized deformation (left, Franklin et al. 2000); typical material response (middle); inverse behaviour of the critical strain (right)

we see that the waviness and roughness of the deformed specimen is increased, so expensive post processing is needed to ensure product quality. In the case of the inverse and normal behaviour of the critical strain, however, the production process can be optimised by avoiding these critical strain rates, where the onset of PLC effect is earliest in process.

2 Experimental Findings

To deal with the PLC effect, tensile tests have been performed. Polycrystalline flat specimens (gage length 21mm, width 5.1mm, thickness 1.55mm) have been

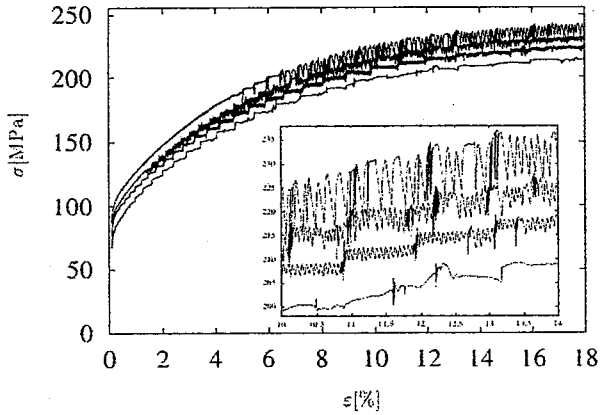

Fig. 2. Comparison between the experimental data of tensile tests for different plastic strain rates. The curves are deliberately shifted along the ordinate axis for clarity. The strain rate from the upper curve downwards are as follows: $2 \cdot 10^{-5} s^{-1}$ [+15MPa], $2 \cdot 10^{-4} s^{-1}$ [+10MPa], $8 \cdot 10^{-4} s^{-1}$ [+5MPa], $6 \cdot 10^{-3} s^{-1}$ [+0MPa].

manufactured from an Al-Mg alloy (AA5754 - Mg 2.6-3.6%). All samples are cut from sheet materials with the tensile axis chosen in the rolling direction. After grinding and polishing, the specimens are annealed for two hours at 400°C and afterwards quenched in water. Tensile tests are performed at room temperature with four different imposed strain rates between $2 \cdot 10^{-5} s^{-1}$ and $6 \cdot 10^{-3} s^{-1}$. The experimental stress-strain curves are shown in Figure 2. With higher strain rates, lower normalized stress-strain curves result, and also the stress drop distribution is depending on applied strain rate, which can be seen in the enlargement.

The three typical statistical characteristics of the stress drop distribution can also be distinguished. For the high strain rate, small stress drops are dominating. For the medium strain rates, two different stress drop amplitudes are dominating, and for the low strain rate, bigger stress drop amplitudes are prevailing. More details about the statistical analysis of stress strain curves are given in for example Lebyodkin et al. (1969), Lebyodkin et al. (2000), Lebyodkin et al. (2001) and Kubin et al. (2002).

3 Micromechanical Mechanisms

Free dislocations become temporarily arrested at obstacles like forest dislocations (Fig. 3). During the waiting time t_w at the obstacles, solute atoms migrate towards the dislocations, condensing in a cloud around the dislocation and producing additional pinning. The pinning force necessary to move the dislocation increases in time t_a and the system ages. As soon as the stress becomes large enough, the pinning breaks down and the dislocation flashes over a distance ω to stop again. Steady pinning and unpinning of the free dislocations from the solute atoms produces the PLC effect.

A detailed interpretation and the theoretical background of the PLC effect can be found in Penning (1972), Kubin and Estrin (1996), as well as Rizzi and Hähner (2004).

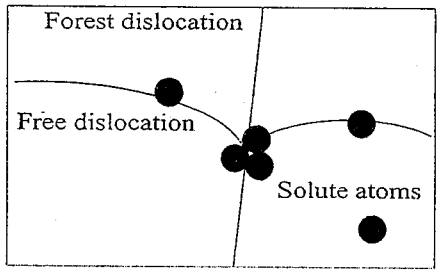

Fig. 3. Interaction of dislocations and solute atoms

4 Modelling of the PLC Effect

In the following, an isotropic elastic viscoplastic material model is formulated which considers large viscoplastic deformations but only small elastic deformations. For the elastic deformations the St. Venant-Kirchhoff law is given by

$$\boldsymbol{\tau} = \boldsymbol{C}\left[\mathbf{E}_e^A\right], \quad \boldsymbol{C} = \lambda \cdot \mathbf{I} \otimes \mathbf{I} + 2G\mathbf{I}^S, \quad \mathbf{E}_e^A = \tfrac{1}{2}\left(\mathbf{I} - \mathbf{B}_e^{-1}\right). \tag{1}$$

The Kirchhoff stress tensor $\boldsymbol{\tau}$ is connected to the elastic Almansi strain tensor $\mathbf{E}_e^A$ by the isotropic stiffness tensor $\boldsymbol{C}$. λ and G denote the Lamé coefficients and $\mathbf{B}_e = \mathbf{F}_e \mathbf{F}_e^{\mathrm{T}}$ the elastic left Cauchy Green tensor. The kinematics are described by

$$\mathbf{L} = \dot{\mathbf{F}}\mathbf{F}^{-1}, \quad \mathbf{D} = \tfrac{1}{2}\left(\mathbf{L} - \mathbf{L}^{\mathrm{T}}\right), \tag{2}$$

where $\mathbf{L}$ is the velocity gradient and $\mathbf{F}$ the deformation gradient. $\mathbf{D}$ denotes the symmetric part of the velocity gradient. The viscoplastic behaviour is given by a von Mises type flow rule for large plastic but small elastic deformations

$$\mathbf{D}_p = \frac{3\dot{\varepsilon}_p}{2\sigma}\boldsymbol{\tau}', \quad L_v(\mathbf{B}_e) = \dot{\mathbf{B}}_e - \mathbf{L}\mathbf{B}_e - \mathbf{B}_e\mathbf{L}^{\mathrm{T}}, \tag{3}$$

$$-\frac{1}{2}L_v(\mathbf{B}_e) = sym\left(\mathbf{L}_p\mathbf{B}_e\right), \quad sym\left(\mathbf{L}_p\mathbf{B}_e\right) \approx \mathbf{D}_p,$$

where

$$\dot{\varepsilon}_p = \sqrt{\frac{2}{3}}\left\|\mathbf{D}_p\right\|, \quad \sigma = \sqrt{\frac{3}{2}}\left\|\boldsymbol{\tau}'\right\|, \quad \boldsymbol{\tau}' = \boldsymbol{\tau} - \frac{1}{3}tr(\boldsymbol{\tau})\,\boldsymbol{I} \tag{4}$$

and the prime denotes the symmetric and traceless part of a tensor.

On the micro scale the PLC effect is produced by additional pinning of dislocations temporarily arrested at localized obstacles (forest dislocation junctions) by diffusing solutes. This mechanism is represented by a scalar flow rule for the equivalent plastic strain rate originally provided by Zhang et al. 2001, modified to adapt it to the material behaviour of the above described Al-Mg alloy. The equivalent plastic strain rate is given by

$$\dot{\varepsilon}_p = \dot{\varepsilon}_o \exp\left(\frac{\sigma - \sigma_d - P_1(\varepsilon_0 + \varepsilon_p)C_s}{S}\right), \tag{5}$$

where $\dot{\varepsilon}_0$, ε_0 and P_1 are constants. σ_d describes the strain hardening and S the strain rate sensitivity effect of the flow stress

$$\sigma_d = d_1 + d_2\left(1 - exp\left(-\frac{\varepsilon_p}{d_3}\right)\right), \quad S = s_1 + s_2\sqrt{\varepsilon_p}\,. \tag{6}$$

The concentration of solute atoms at pinned dislocations is

$$C_s = \left(1 - exp\left(-P_2 t_a^n\right)\right) C_m \tag{7}$$

and depends on the accumulated plastic strain ε_p and the aging time t_a which is an internal variable

$$\dot{t}_a = 1 - \frac{t_a}{1_w}, \quad t_w = \frac{\Omega}{\dot{\varepsilon}_p}, \quad \Omega = \omega_1 + \omega_2 \varepsilon_p^{\beta}\,. \tag{8}$$

The aging time t_a is the time available to solute atoms to diffuse to dislocations. The rate of change of t_a depends on t_a and the waiting time t_w, the time a dislocation spends at localized obstacles before it unpins.

In order to solve the differential equations, the backward Euler method is used with the assumptions that the initial conditions are $\varepsilon_p(t = 0) = 0$, $t_a\,(t = 0) = 0$. The material parameters are fitted to the experiments by using the hardening behaviour of the

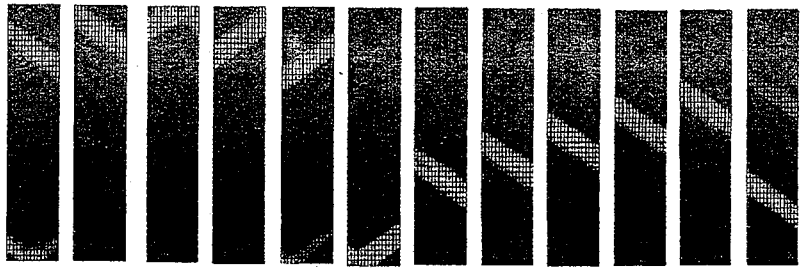

Fig. 4. FE simulation of PLC band propagation

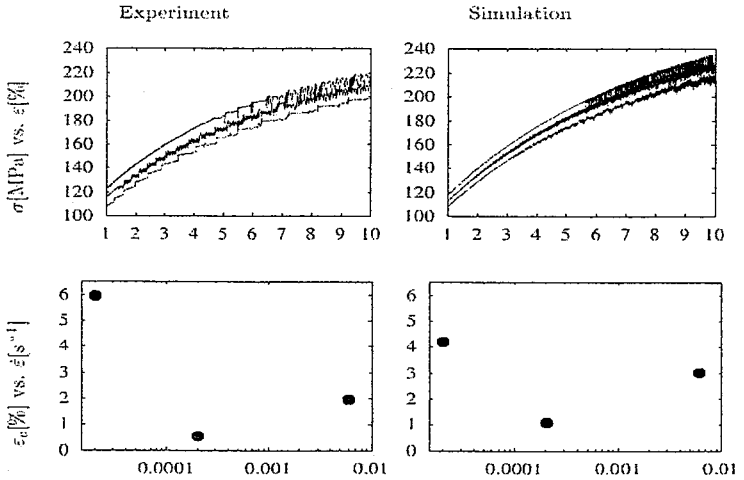

Fig. 5. Comparison of experimental findings with numerical results: σ vs. ε. The curves are deliberately shifted along the ordinate axis for clarity. The strain rate from the upper curve downwards are as follows: $2 \cdot 10^{-5}s^{-1}$ [+10MPa], $2 \cdot 10^{-4}s^{-1}$ [+5MPa], $6 \cdot 10^{-3}s^{-1}$ [+0MPa] (top) and ε_c vs. $\dot{\varepsilon}$ (bottom).

normalized stress strain curves for the hardening parameters. For the parameters describing the aging behaviour the stability analysis of the strain rate sensitivity of the stress is used. The material parameters of the above model for the Al-Mg alloy (*AA5754*) are listed in the table below.

5 Comparison of Experimental Findings with Simulation

In Figure 5 and 6 the experimental findings are compared to the numerical results.

The hardening behaviour is reproduced well. The different types of serrations observed experimentally are recovered by the simulation. The comparison of the statistical behaviour (Fig. 6), such as the stress drop distribution function shows acceptable agreement. The shift from type A for high strain rates, where small stress drops magnitudes are dominating, to type B for medium strain rates, to type C for small strain rates, where bigger stress drop magnitudes occur, can be reproduced.

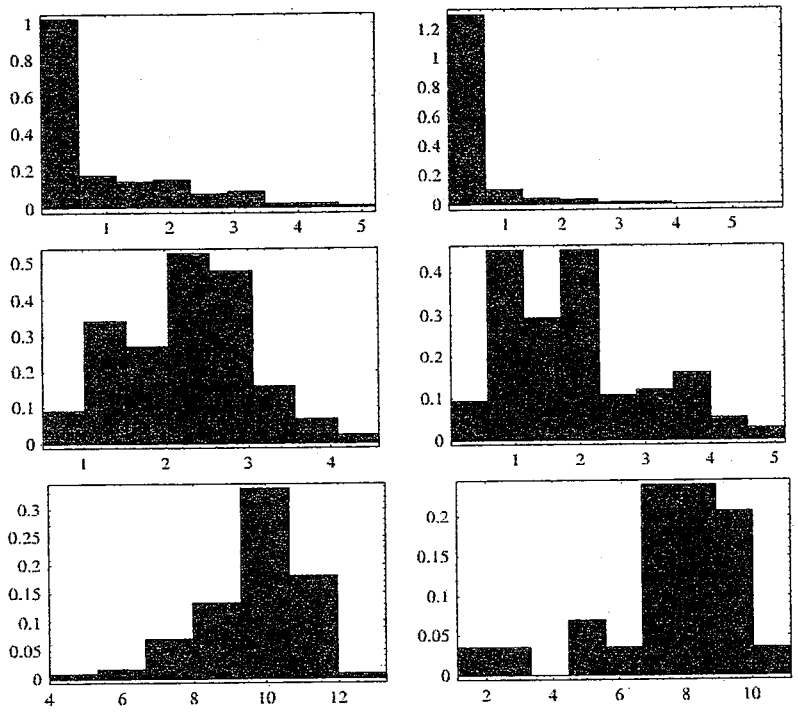

Fig. 6. Comparison of the stress drop distribution function (probability P vs. stress drop amplitude $\Delta\sigma$) for experimental (left) and simulation (right) results, for the stress strain curves of three different imposed strain rates, $6{\cdot}10^{-3}s^{-1}$ (top), $2{\cdot}10^{-4}s^{-1}$ (middle), $2{\cdot}10^{-5}s^{-1}$ (bottom)

Another characteristic feature is the critical strain ε_c , which is shown in Figure 5 (bottom). With the current material model this effect can also be reproduced in general.

To ensure that the results are not depending on the finite element mesh size, simulations have been performed with three different numbers of elements, 10, 30 and 150 (Fig. 7). The results show good agreement concerning the hardening behaviour and the onset of jerky flow, but the statistical behaviour of the serrations shows differences, in particular for small strain rates.

Table 1. Material parameters of an AlMg alloy

parameter	value	parameter	value
P_1	325.0	d_1 (MPa)	75.0
P_2 ($s^{1/3}$)	4.0	d_2 (MPa)	165.0
β	1.0	d_3	$7.0\ 10^{-2}$
ω_1	$1.0 \cdot 10^{-6}$	E (MPa)	70000
ω_2	$1.0 \cdot 10^{-4}$	ν	0.3
s_1 (MPa)	0.41	ρ (kg/m^3)	2650
s_2 (MPa)	2.91	$\dot{\varepsilon}_0$ (s^{-1})	$2.3\ 10^{-7}$
n	1/3	ε_0	0.001

6 Further Numerical Results Compared to Experimental Findings in the Literature

In the literature other experimental results concerning the PLC effect in different deformation processes of the alloy Al-Mg are listed. For example, stress rate driven tests are performed by Kovacs et al (2000). The test results with a stress rate of 0.5MPa/s is reproduced by the simulation and shows a comparable hardening behaviour and the typical steps for stress rate driven tests, but the onset of the PLC effect is predicted to late by the simulation. One possible reason for this may be the different Mg concentration and the different solution heat treatment temperatures. Also, compression test results can be found for an Al-Mg alloy in Horvath et al (2007). Tests are performed at three different stress rates, 0.02, 0.2 and 3MPa/s. Simulation results can reproduce the hardening behaviour in general (Fig. 7, right).

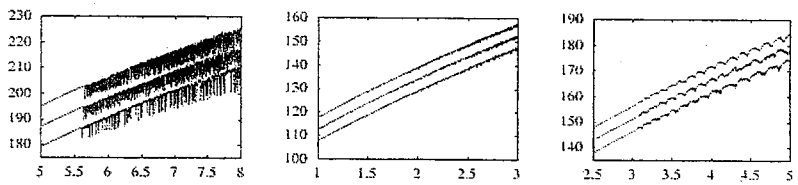

Fig. 7. σ vs. ε comparison of numerical results produced ($2{\cdot}10^{-5}s^{-1}$ (right), $2 \cdot 10^{-4}s^{-1}$ (middle), $6 \cdot 10^{-3}s^{-1}$ (right)) by using 10 (bottom), 30 (middle) and 150 (top) elements in the FE model. The curves are deliberately shifted along the ordinate axis for clarity.

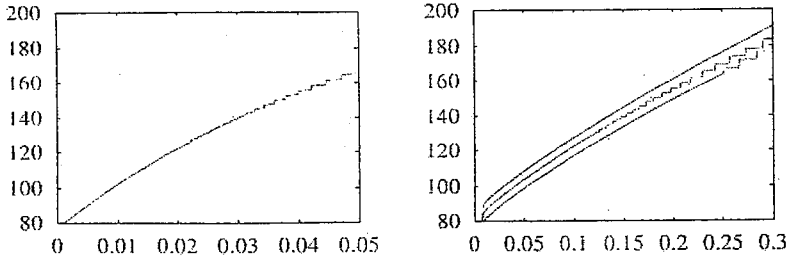

Fig. 8. Examples of numerical results σ vs. ε for stress rate driven (left) and compression tests with different stress rates (right). The curves are deliberately shifted along the ordinate axis for clarity.

After the literature and also in the simulations, the different tested stress rates have hardly any influence on the hardening behaviour. And the typical steps for stress driven tests are shown too. The differences for the onset of serrations may occur in the compression tests also due to different Mg concentrations and different solution heat treating temperatures.

7 Conclusions

FE simulations have been performed with a 3D isotropic, geometrically nonlinear PLC model. Material parameters have been identified, and the results of the simulations compared with experimental findings. The comparison of experiment with simulation shows good agreement for the strain hardening behaviour and the statistical behaviour of the stress drops for all strain rates. Also the inverse effect of the onset of instability could be reproduced by this material model. Simulation results of experimental data in the literature are shown.

Acknowledgments. The authors gratefully thank Y. Estrin (TU Clausthal, Institut für Werkstoffkunde und Werkstofftechnik) and M. Lebedkin for the possibility of performing the deformation tests and many helpful discussions.

References

[1] Lebyodkin, M., Dunin-Barkowskii, L., Lebedkina, T.: Statistical and multifractal analysis of collective dislocation processes in the Portevin-Le Chatelier effect Physical. Mesomechanics 4, 9 (2001)
[2] Kubin, L., Fressengeas, C., Ananthakrishna, G., In Nabarro, F., Duesbery, M.: Collective Behaviour of Dislocations in Plasticity. Dislocations in Solids 102 (2002)
[3] Zhang, S., McCormick, P., Estrin, Y.: The morphology of Portevin-Le Chatelier bands: finite element simulation for Al-Mg-Si. Acta. Mater. 49, 1087 (2001)
[4] Horvarth, G., Chinh, N., Gubicza, J., Lendvaih, J.: Plastic instabilities and dislocation densities during plastic deformation in Al-Mg alloys. Mat. Sci. Eng. A445(446), 186 (2007)

[5] Kovacs, Z.s., Lendvai, J., Vörös, G.: Localized deformation bands in Portevin-LeChatelier plastic instabilities at a constant stress rate. Mat. Sci. Eng. A 279, 179 (2000)
[6] Franklin, S.V., Mertens, F., Marder, M.: Portevin-Le Chatelier effect. Physical Review E 62, 8195 (2000)
[7] Bross, S., Hähner, P., Steck, E.A.: Mesoscopic simulations of dislocation motion in dynamic strain ageing alloys. Computational Materials Science 26, 46 (2003)
[8] Marciniak, Z., Kuczynski, K.: Limit Strains in the processes of stretch-Forming sheet metal. Int. J. Mech. Sci. 9, 609 (1967)
[9] Lebyodkin, M., Brechet, Y., Estrin, Y., Kubin, L.: Statistical behaviour and strain localization patterns in the Portevin-Le Chaterlier effect. Acta mater 44, 4531 (1996)
[10] Lebyodkin, M., Dunin-Barkowskii, L., Brechet, Y., Estrin, Y., Kubin, L.P.: Spatio-temporal dynamics of the Portevin-Le Chatelier effect: experiment and modelling. Acta mater. 48, 2529 (2000)
[11] Rizzi, E., Hähner, P.: On the Portevin-Le chatelier effect: theoretical modeling and numerical results. Int. J. Plast. 20, 121 (2004)
[12] Penning, P.: Mathematics of the Portevin-Le Chatelier effect. Acta Metall. 20, 1169 (1972)
[13] Estrin, Y., Kubin, L.: Spatial Coupling and propagative plastic instabilities. Continuum models for Materials with Microstructure 365 (1995)

Albrecht Bertram
Jürgen Tomas

Micro-Macro-Interactions

In Structured Media and Particle Systems

Springer